AIMS Mathematics, 9(5): 13224–13244.
DOI: 10.3934/math.2024645
Received: 27 January 2024
Revised: 20 March 2024
Accepted: 01 April 2024
Published: 10 April 2024

https://www.aimspress.com/journal/Math

Research article

Research on characteristic quantity and intelligent classification prediction of metal magnetic memory detection signal

Kai Guo[1,*], Chencan Sun[1], Wenjie Pan[2], Wenying Fan[1] and Hongsheng Zhang[1,*]

[1] School of Environmental and Chemical Engineering, Yanshan University, Hebei 066004, China
[2] Zhejiang Academy of Special Equipment Science, Hangzhou, Zhejiang 310020, China

* **Correspondence:** Email: kguo@ysu.edu.cn, zhsysu@126.com; Tel: 8615222819055; Fax: 8603358061569.

Abstract: Metal magnetic memory (MMM) is an innovative, nondestructive testing method. It can detect both stress concentrations and macroscopic defects. The three-dimensional force-magnetic coupling model was established by the ANSYS simulation software, the evolution process of different defect depths was studied in detail, and the change of the signal characteristic was analyzed. The results showed that the variation trend and amplitude characteristic of MMM signals resulted in obvious differences among different defect types. Meanwhile, the impacts caused by the defect parameters and the type are complex, which cannot be decoupled or calculated by a certain formula. The accuracy of the simulation data was verified by experiments. To solve the classification prediction problem in MMM detection, the signal peak and valley $H_{p\text{-}v}$, the signal width W, the gradient K_y, and the peak energy H_y were selected as characteristic parameters to evaluate different defect types according to the change in the signal waveform. Finally, using these vectors as the input variables, the radial basis function neural network (RBFNN) pre-classification test model was established to realize the classification recognition of pit defects, crack defects, and porosity defects. The results show that the accuracy of the training and test sets, and it is feasible to use this model to complete the intelligent classification of defects.

Keywords: metal magnetic memory detection; stress concentration; defect classification; radial basis function neural network; prediction
Mathematics Subject Classification: 65K05, 68T11

1. Introduction

With the promotion of natural gas and hydrogen energy [1], pipeline transportation has been widely used because of its advantage in distance and efficiency. Since the pressure pipe remains in the load state for a long time, it is easy to cause an increase in local stress concentration and regional corrosion. Therefore, it is very necessary to detect and monitor the condition maintenance and structural integrity management of in-service pipelines and pressure vessels [2].

In order to protect the pipeline, non-destructive testing (NDT) methods have been extensively studied. Among them, the metal magnetic memory (MMM) detection technology [3,4] is an effective in- service method without external electric or magnetic fields. Meanwhile, MMM [5,6] detection has a certain sensitive property for failure and a region of stress concentration of ferromagnetic materials [7,8]. Although MMM can quickly and accurately find the location of defects, it cannot make quantitative analyses of the size and type of the defects, which is an important issue in the NDT area.

Characteristic quantities and pattern recognition are two important steps of defect detection using MMM detection technology. Extracting correct defect information is the key to complete intelligent recognition. In the selection of characteristic quantities, Di et al. [9] used the characteristics of wavelet packet energy information to establish a back propagation neural network (BPNN) and realize the identification of weld cracks. Chen et al. [10] used the magnetic total gradient modulus to judge the damage and the location of the damage region boundary, which could effectively identify the damage state according to the vertical characteristics of the magnetic memory signal. Shi et al. [11] established a BPNN network to identify the damage region by using four variables: the original signal energy H_s in the sample center, the gradient energy K_s in the sample center, the mutation width L_w of the original signal in the sample center, and the average absolute gradient value K_{ave}.

In recent years, the combination of traditional nondestructive testing technology and artificial intelligence to improve the accuracy and sensitivity of pipeline defect detection has attracted wide attention. P. Ramuhalli [12] and A. Joshi et al. [13] introduced the radial basis function neural network (RBFNN) to predict the 3D profile of the defect according to the magnetic flux leakage (MFL) detection signal, and then predicted the maximum allowable operating pressure (MAOP) of the pipeline transmission. Zhang et al. [14] built a two-dimensional model of pipeline defects using the ANSYS software and made different defects. The improved particle swarm optimization algorithm (IPSO-RBFNN) was tested, and the size of the pipeline defects was identified. Wang et al. [15] organically combined a principal component analysis (PCA) with a genetic algorithm optimized neural network (GA-BP) method for data processing. The algorithm could effectively approximate the complex nonlinear relationship under the force magnetic coupling and realized the quantitative recognition of magnetic memory signals. Xing et al. [16] introduced the dynamic fuzzy clustering algorithm (DFCA), obtained the initial fuzzy clustering by the output threshold λ, which was further optimized by the immune algorithm, obtained the optimal threshold λ, and finally established an immune-optimized dynamic fuzzy clustering model to predict the damage grade with an accuracy of 90%. Shi et al. [17] established the target defect function and performed the defect inversion.

In the nondestructive testing of pressure vessels or pipelines, it is always an important direction to determine the shape, size, and type of defects according to the information of detection signals for the development of nondestructive testing. However, the effect of the shape, size, and type of defects can be mixed together, which makes it difficult to realize the defect classification and characteristic quantities. In this paper, a comprehensive study on the defect classification and characteristic quantities of MMM tests are performed through numerical simulations and experiments. Based on the change of the defection signal, the defect characteristic is analyzed considering different defect types and sizes,

and the data sets of the defect characteristic are built to perform an intelligent classification prediction. Then, the RBFNN is established to predict the defect type. This research can be an important reference and guidance of the intelligent classification of NDT signals based on a neural network.

2. Materials and methods

2.1. Materials

Q235C was used as the experiment and simulation of the test material, which is a kind of ferromagnetic steel plate widely used in mechanical engineering as pipelines and pressure vessels due to its good welding and processing performances. The detailed properties are shown in Table 1. The material is used in the simulation and experiments.

Table 1. Material properties of test specimen.

(a) Chemmiacal content;

Element	C	Mn	P	S	Si	Fe
Content(%)	0.20	1.4	≤0.03	≤0.03	0.035	bal

(b) Properties.

Property	Density (kg/m^3)	E (GPa)	σ_s (MPa)	Relative permeability	Conductivity (S/m)
value	7850	200	235	285	$2.96x10^6$

2.2. Methods

Although MMM detection can quickly and accurately locate the position of defects, it cannot perform pattern recognition to predict defect types. To solve this problem, this paper combines MMM detection and RBFNN to save the detection time, simplify the detection process, and make the detection technology more intelligent. The intelligent quantitative analysis is mainly divided into two parts. The first part obtains the magnetic memory signal law under different defect types. The second part establishes the RBFNN, including the training adjustment and the determination of parameter values.

2.2.1. Numerical method

To obtain the stress and magnetic field of the MMM testing, a numerical simulation is adopted to study the signals and build the data set for the neutral network. The form of "permanent magnet + Yoke" [18] was used to simulate the magnetic field intensity distribution of the specimen in the geomagnetic field environment. The relative permeability of the armature was 186000, and an external air layer was established to wrap it, as shown in Figure 1(a). The specimen utilized Q235C as the ferromagnetic material, the size of the specimen was 100×20×6 mm, and there were three kinds of defects in the middle of the specimen: pit defects, crack defects, and porosity defects. The crack defect is shown in Figure 1(b), where the depths of crack defects are 1, 2, 3, 4, and 5 mm, respectively. The radius of the pit is 2 mm, and the depth of the pit is h (1,2, 3, 4, 5, and 6mm), as shown in Figure 1(c).

The depths of the porosity defects are similar to the crack defects.

The general process of the simulation is shown in Figure 2. The SOLID185 unit is used in the mechanical simulation stage, and the SOLID96 unit is used in the magnetostatic simulation stage, both of which are hexahedral eight-node units, which can complete the calculation of force-magnetic coupling. Intelligent grid division is adopted, and the mesh is encrypted to 0.5 mm around the defect location of the specimen. The magnetic field strength at the specimen location is similar to that of the geomagnetic field, and its value is around 40 A/m [19], which meets the calculation requirements and can be used for numerical simulation calculation.

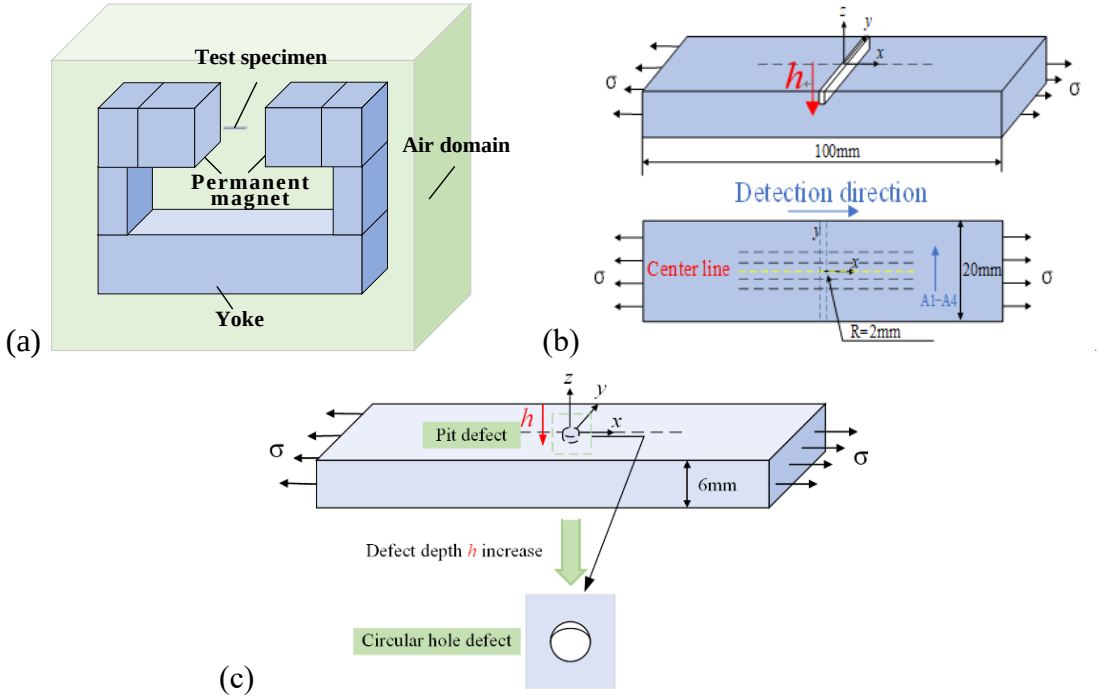

Figure 1. Analysis model. (a) Geomagnetic field model; (b) specimen size; (c) the pit defect expands along the depth *h* direction.

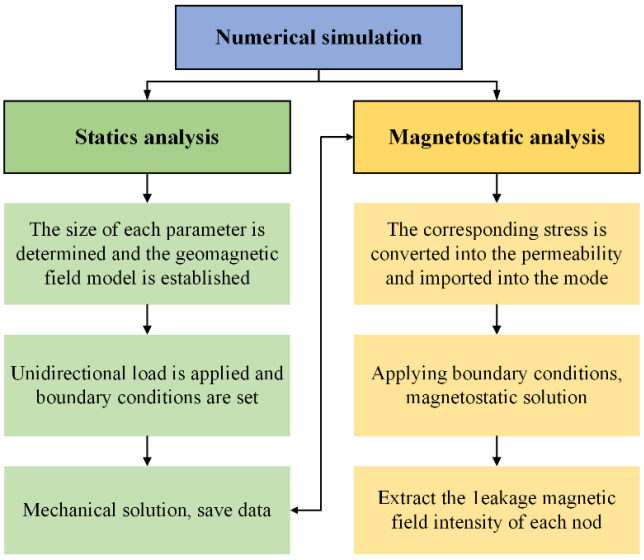

Figure 2. Numerical simulation of MMM detection.

In the static stage, in order to simulate the static load unidirectional tensile, the middle part of the specimen model that contains defects is subjected to displacement constraints, and the stress is applied to both ends of the specimen to solve the stress. The permeability values corresponding to the stress values in different elements are calculated through the coupling formula [20] of the force-magnetic relationship and are stored in the post-processing model. In the magnetostatic stage, the permeability corresponding to each element in the array is imported into the specimen model, where B_m=2T, λ_m=40×10^{-6} [21], μ=285H/m [22], and σ=100MPa in the linearized equation. The solution of the static magnetic field can be realized by applying boundary conditions to the outermost air and using the magnetic vector method to load the analysis model. We extract the magnetic field intensity components of each node on the path to obtain the distribution law of the surface leakage magnetic field in post-processing.

2.2.2. Experiment method

The experiment aims to verify the simulation and accumulate the testing data. As shown in Figure 3, the universal testing machine model WDW-100G is used in this experiment for the static load tensile test, and the detector model EEC-2003+ is used for metal magnetic memory detection. The material of the specimen is Q235C. The size of the specimen is 100×20×6 mm. Either a pit or a crack defect is prefabricated in the middle of the specimen. The depth h of the pit defect is 1, 2, 3, 4, and 5 mm, respectively. The depth h of the crack is 1,2, 3, and 4 mm, respectively, and the defect width is 4 mm.

A magnetic memory detector adopts a pen style probe and uses a stepper motor screw group to control the moving speed and distance of probe and to prevent an inaccurate measurement caused by a jitter. Pulse counting is realized by using the internal clock timing, the suppressed geomagnetic field is set, and then the earth upward and downward calibration is established. Using online detection, the test force of loading is 10 kN, the force control loading method is adopted, and the speed is 0.05 kN/s. When the target force is stable, the probe is vertically pressed to the surface of the specimen, the stepper motor drives the probe to move, and the speed of the probe is 3mm/s.

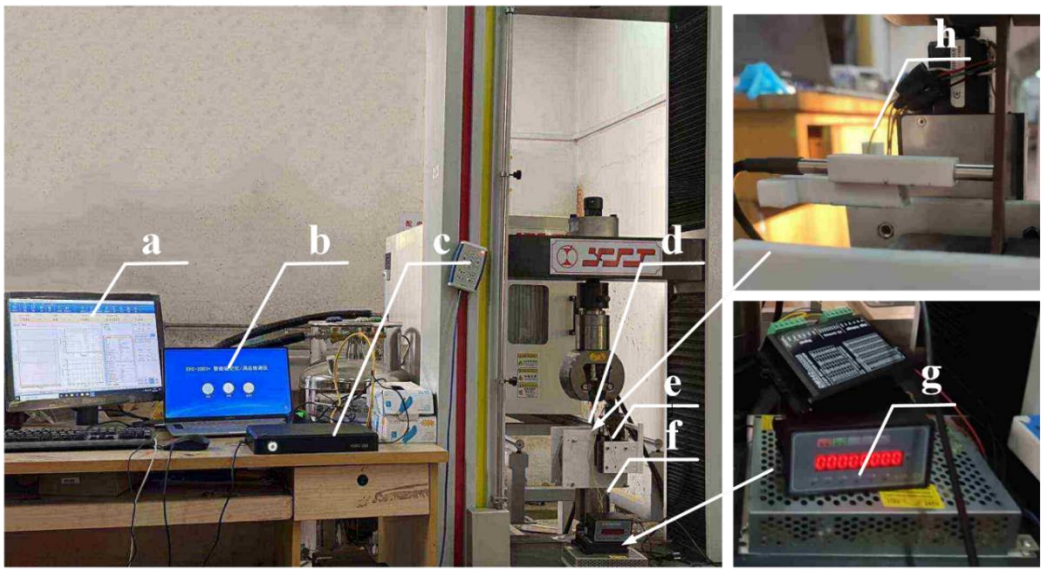

Figure 3. Experimental facility. (a) Drawing machine control interface; (b) upper computer; (c) EEC-2003+ Detector; (d) test specimen; (e) stepper motor; (f) stabilizing device; (g) controller; (h) test probe.

2.2.3. Intelligent recognition method

The defect type classification is difficult to realize, and the neutral network can be an effective tool to solve this problem. RBFNN has the advantages of a single hidden layer, a simple structure, and a strong nonlinear approximation ability; moreover, it is widely used in pattern classification and recognition. Considering that it is impossible to classify and identify defects by solely relying on MMM detection, magnetic memory signals contain rich information of characteristic quantities. By combining RBFNN and MMM detection, the function of MMM detection in defect prediction is further played through the characteristic quantity of the signal. RBFNN is a three-layer neural network: The first layer is the input layer, and the number of nodes is determined by the dimension of the input signal; the second layer is the hidden layer, which seeks to complete the transformation of the input signal to the hidden layer space, where the number of nodes is composed of radial basis function; and the third layer is the output layer, where the nodes are determined by the basis function given by the hidden layer. Its topology is shown in Figure 4.

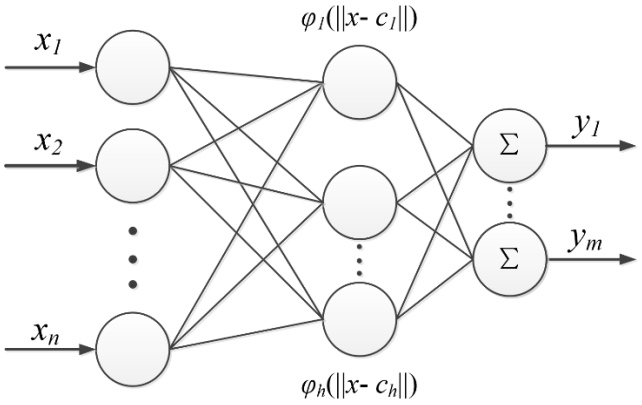

Figure 4. RBFNN topology.

As shown in Figure 4, the RBFNN structure is *n*-*h*-*m*, that is, the network has *n* input nodes, *h* hidden nodes, and *m* output nodes, where $x=[x_1,x_2,\ldots,x_n]^T \in R^n$ is the input vector of the network, $\boldsymbol{W}\in \mathbf{R}^{h\times m}$ is the output weight matrix, $y=[y_1,\ldots,y_n]^T$ is the output, $\varphi_i(\bullet)$ is the activation function of the *i* th hidden node, and c_i is the data center value of the *i* th hidden node in the network. $\|\bullet\|$ represents the distance between the input and the center vector.

RBFNN is a feedforward neural network based on the radial basis function, which is different from traditional perceptron neural networks in that uses radial basis functions instead of conventional activation functions. The radial basis function is a training function based on distance. Its basic principle is to measure the distance between the input vector and the center point and convert it into the output value. It has a strong approximation ability and a fast training speed. Its training process is usually completed in two steps: the first step is to determine the position of the center point through an algorithm, and the second step is to determine the weight using either the least square method or the gradient descent method.

It is well known that MMM detection has an extreme value of tangential components and a zero crossing of normal components [24]. However, in the actual environment, it is easy to be disturbed by noise, and the normal component may drift, which is easy to cause misjudgment or a missing judgment. Additionally, there are some characteristic variables for magnetic memory signals. The input vector is

composed of representative characteristic variables, and the defect type is intelligently identified by RBFNN to make up for the shortcomings of metal magnetic memory detection in the qualitative analysis and the defect recognition. The characteristic variables are as follows:

(1) Peak-trough value of magnetic memory normal component $H_{p\text{-}v}$:

$$H_{\text{p-v}} = \text{peak of wave } H_P(y) - \text{valley of wave } H_P(y). \tag{1}$$

(2) Magnetic memory normal component wave width W.

(3) Magnetic memory signal gradient K_y:

$$K_{\text{y}} = \max \Delta H_P(\text{y}_\text{i}) / \Delta x_i. \tag{2}$$

(4) Peak energy at the signal break H_y:

$$H_y = \int_{x_1}^{x_2} \{|H_p(y) - ave(H_p(y))|\} dx. \tag{3}$$

RBFNN has the advantages of a simple structure and a strong learning ability. The neural network completes the classification and recognition of unknown defects by training known data, as shown in the figure below. The magnetic memory signal obtained by numerical simulation and the data in the literature are preprocessed to obtain the parameter variables that represent the defect characteristics, which constitute the input vector $\{H_{p\text{-}v}; W; K_y; H_y\}$.

The defect identification process is shown in Figure 5. Input vectors of the database are read, data sets are scrambled, training and test sets are divided, and the data is normalized. Then, the expansion rate of the radial basis function and other parameters are set up, and RBFNN is built to test the neural network. The data is processed by reverse normalization. Simulations can test the network. Finally, the output results are three defect types: pit defects, crack defects, and porosity defects. According to the above process, the intelligent identification of defects is realized. In the actual engineering inspection, it can realize the real-time detection and measurement of in-service equipment, and the defect location and defect type are known, so as to realize the real-time monitoring and defect prevention of an equipment failure.

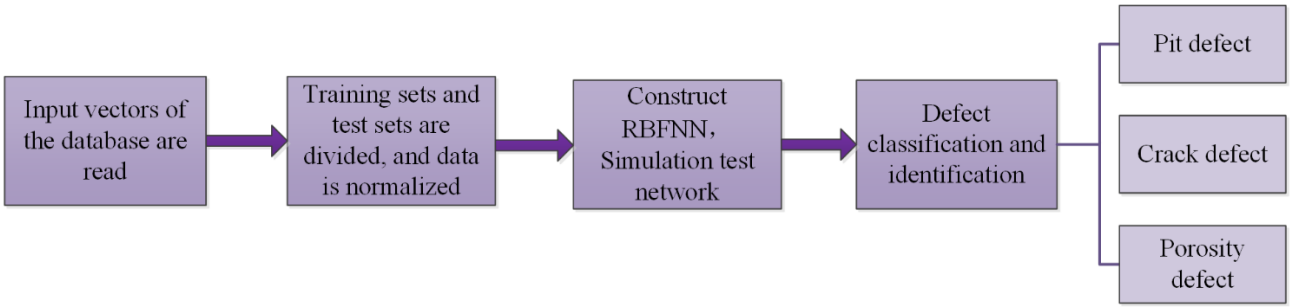

Figure 5. Defect classification process.

3. Results

3.1. Pit defects

3.1.1. Effect of defect depth

The Mises stress distribution of the specimen under 100 MPa stress at the pit defect is shown in Figure 6, from which it can be seen that the stress near the pit presents a "butterfly" distribution, and the maximum value of the stress amplitude appears at the inner side of the pit. The Mises stress amplitude at the outer edge of the notch is smaller than what is measured inside, and the closer one gets to the defect location, the higher the degree of the Mises stress concentration and the Mises stress amplitude. The peak of the MMM signal in the tangential and normal signals is consistent with the amplitude in the Mises stress distribution. With the increase of the defect depth, the range of the Mises stress concentration along the length of the specimen gradually expands, and the larger the stress concentration amplitude, the greater the increase in the magnetic memory signal. The stress distribution is consistent with the law in reference [25].

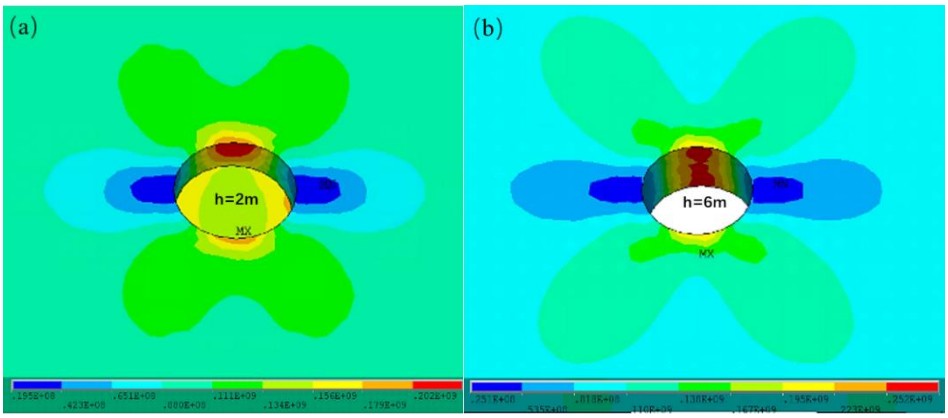

Figure 6. Mises stress distribution. (a) h=2mm; (b) h=6mm.

The tangential magnetic field strength and the normal magnetic field strength as functions of the scan displacement when the defect depth is 1, 2, 3, 4, 5, and 6 mm, respectively, are shown in Figure 7. When the defect is 1 mm, as the tangential and normal components change, the extreme value of the tangential component occurs, and the zero-crossing point of the normal component can be observed at the defect position. The edge signals of the defect can also appear. The depth of the defect h gradually increases, the change of the magnetic memory signal gradually increases, and the normal component appears in "reverse", which is similar to the reference [23]. When the defect is large enough to traverse through the entire thickness, the magnetic memory signal sharply increases, the tangential component has a minimum value in the center of the pit, two maximum values appear at both ends of the diameter, and the normal component has a "reverse" situation.

The normal magnetic field component is highly sensitive to the defect location, and the gradient signal is obtained by processing the normal magnetic field intensity, as shown in Figure 8(a). The metal magnetic gradient near the stress concentration zone of the sample, namely the necking point, is much larger than the other area [26–28]. The gradient value has extreme value points at the location of the defect, and the extreme value points exist at both ends of the diameter and the geometric center based on the dimensional characteristics of the defect. Due to the action of the external load, the local stress

concentration is more serious, the normal magnetic field intensity appears as an “abrupt change” near both ends of the crater diameter, and the gradient value of the abrupt change increases with an increase of the defects. At the geometric center of the defect, the gradient value decreases, but the amplitude of the change increases. Furthermore, the peak energy change around the defect is shown in Figure 8(b).

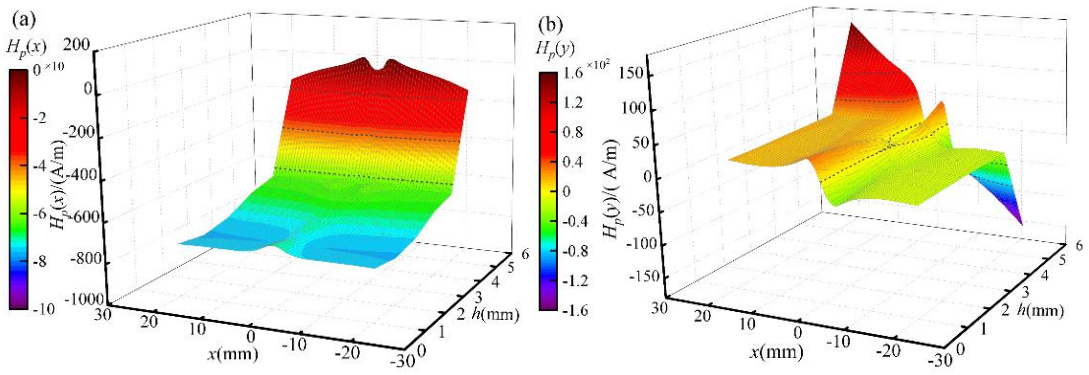

Figure 7 The magnetic field strength of circular pit defects. (a) Tangential magnetic field strength; (b) Normal magnetic field strength.

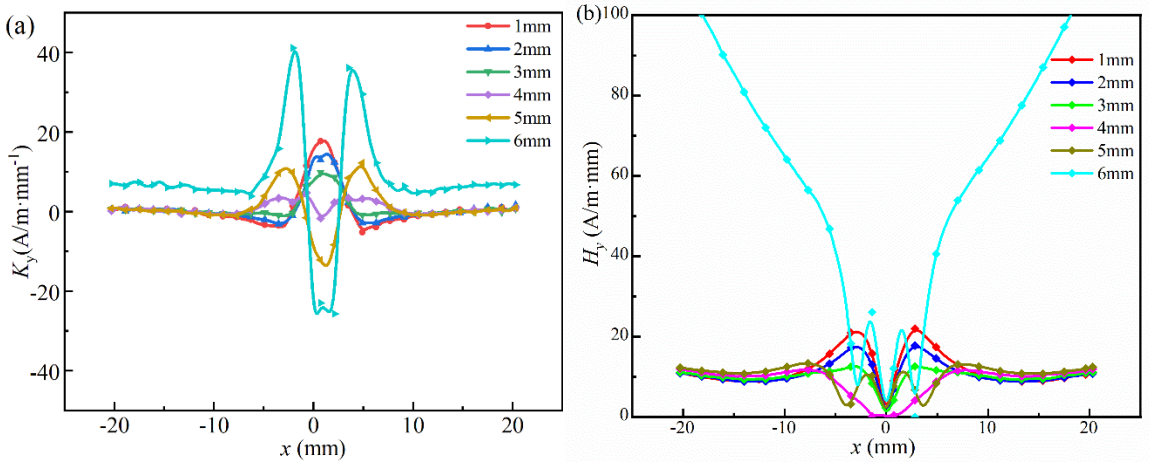

Figure 8. The normal magnetic field characteristic of pit defects. (a) Normal magnetic field gradient; (b) Normal magnetic field peak energy.

The change of the normal magnetic field energy can be roughly divided into three stages when the pit defect is extended from 1 mm to the through-hole. In the first stage, when the defect depth is 1–3 mm, the normal magnetic field energy at the defect position gradually weakens, and the normal magnetic field strength has a minimum value. In the second stage, when the defect depth is 4–5 mm, the normal magnetic field energy continues to decrease. When the defect increases to 5 mm, the normal magnetic field intensity has two extreme values at both ends of the circular diameter. In the third stage, the normal magnetic field energy increases and the fluctuation range increases when the defect becomes a through-hole. By observing the overall curve, it can be seen that the normal peak energy amplitude gradually decreases around the defect.

The signal on the surface of the specimen gradually increases when the depth of the pit defect increases. When the pit evolves into a through-hole, the signal energy is significantly different compared to other depths. Near the defect, as the defect depth increases, the energy of the magnetic

memory signal gradually decreases, and the sharp change of energy is exactly at the two ends of the diameter. Therefore, the range of the damage area and defect location can be indirectly reflected by analyzing the change of the signal peak energy.

3.1.2. Effect of pit size

The Mises stress distribution near the defect is shown in Figure 9, where the depth of the pit defect is h=2 mm and the radius R=1 is 5 mm. The Mises stress around the pit presents a "butterfly" distribution, and the amplitude of the Mises stress exists inside the pit defect. An increase of the radius R leads to a more prominent "butterfly shape", and the stress degree is more concentrated. The location of the Mises stress amplitude corresponds to the location of the sudden change in the magnetic memory signal.

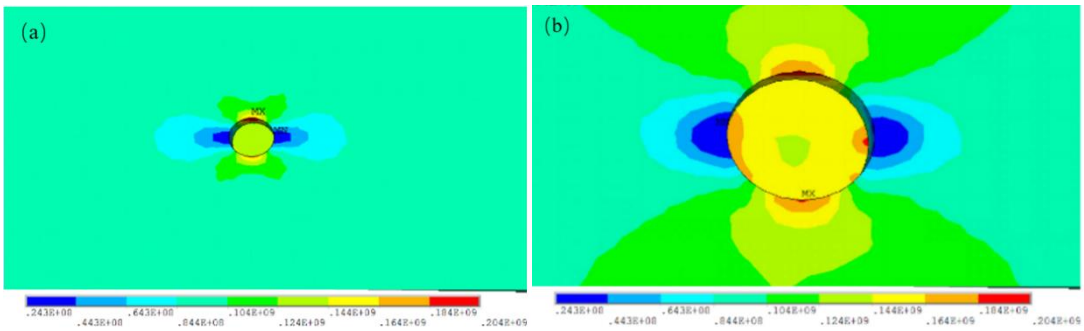

Figure 9. Mises stress distribution. (a) R=1 mm; (b) R=5 mm.

In order to study the influence of the pit defects width on the magnetic memory signal, similar specimen sizes and loading methods were adopted. The defect radius R was 1, 2, 3, and 4 mm. The magnetic memory signal obtained is shown in Figure 10. For the tangential component of the magnetic memory signal, the defects do not regularly change. For the tangential component of the magnetic memory signal, with an increase of the defect width, the magnetic memory signal gradually weakens, the amplitude of the signal decreases, and the waveform of the signal has a trend of an outward expansion.

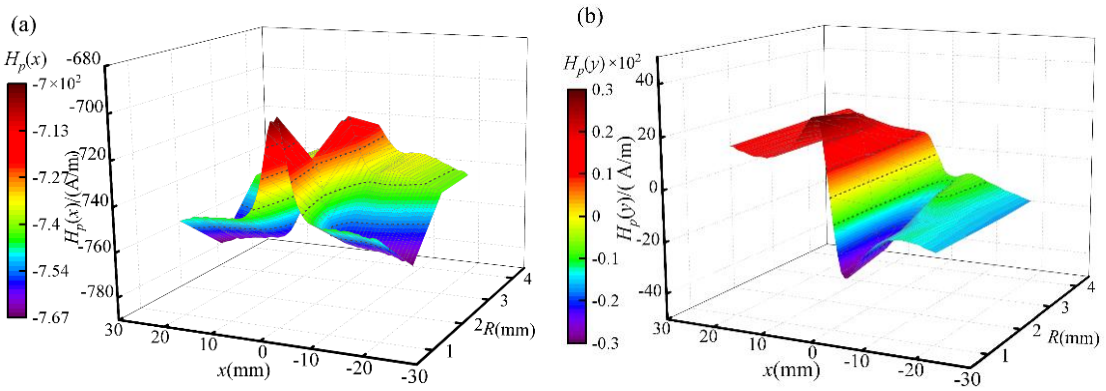

Figure 10. The magnetic field strength of pit defects. (a) Tangential magnetic field strength; (b) Normal magnetic field strength.

As shown in Figure 11(a), the gradient amplitude of the normal signal gradually decreases with an increase of the defect width, and the gradient amplitude presents a nonlinear change. Similarly, as shown in Figure 11(b), the peak energy of the signal gradually decreases with an increase of the defect width. Compared with the defect depth, the defect width has less of an influence on the magnetic memory signal, though it also has the rule of the magnetic memory signal. The variation trend of the magnetic memory signal of the defect width is similar to that of the depth. Therefore, only the effect of the defect depth is discussed in the following sections for crack and porosity defects.

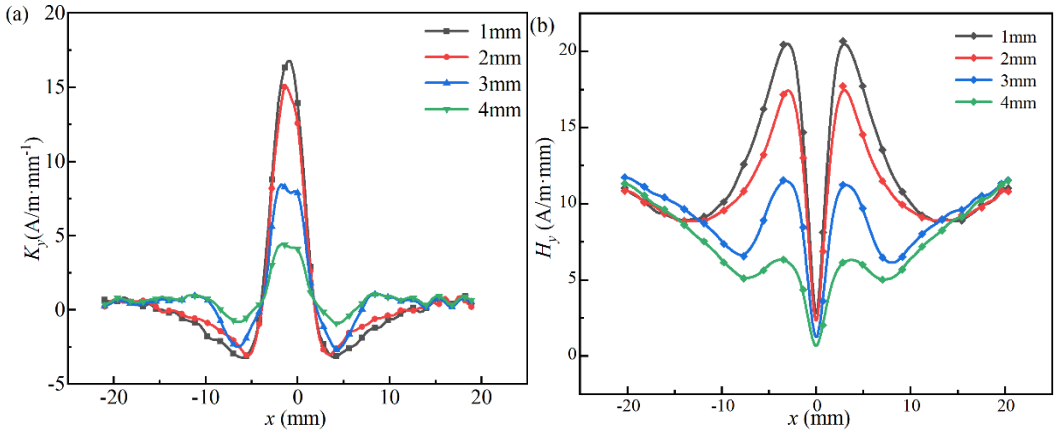

Figure 11. The normal magnetic field characteristic of pit defects. (a) Normal magnetic field gradient; (b) Normal magnetic field peak energy.

3.2. *Crack defects*

A crack defect is the most important defect in the pipeline, and is not easy to be found in the practical detection. The Mises stress distribution near the crack is shown in Figure 12, in which the stress is 100 MPa. When the defect depth is 1mm, the peak stress appears inside the crack and spreads from inside to outside, and a "fishtail" shape appears at the crack end. With a increase of the defect depth, the specimen has a small deformation, the Mises stress concentration at the crack is enhanced, and the Mises stress amplitude increases. The position of the Mises stress amplitude coincides with the sudden change of the magnetic memory signal. The peak value of the magnetic memory signal comes from the two edge locations of the stress concentration, which is also reflected in the reference [16].

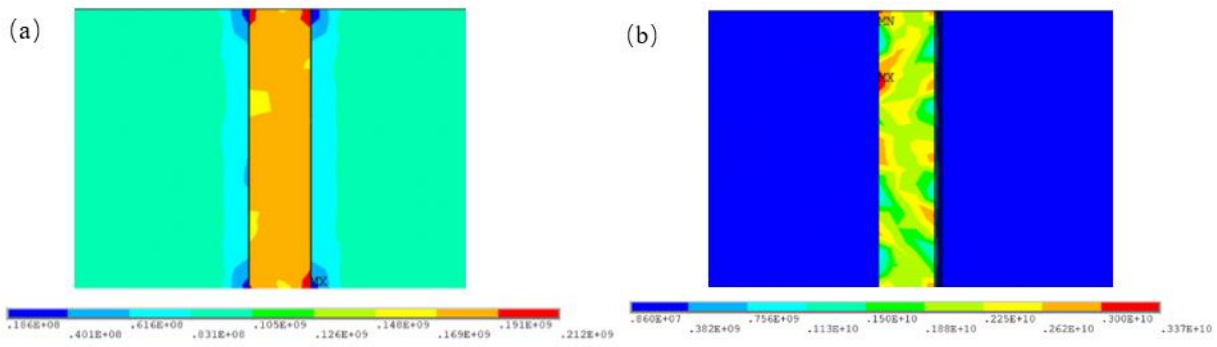

Figure 12. Mises stress distribution. (a) h=1mm; (b) h=5mm.

Magnetic memory signals of crack defects with different depths are shown in Figure 13. The defect depths are 1, 2, 3, 4, and 5 mm, respectively. Generally, the defect location can be accurately located by the tangential and normal components of the magnetic memory. The variation range of the magnetic memory signal is much lower when the defect depth is smaller than 2 mm. When the defect depth increases to 1/2 of the plate thickness, the peaking and valley changes of the tangential and normal components are larger than that of the pits, and the defect signal shows an obvious "reverse" phenomenon in the normal component.

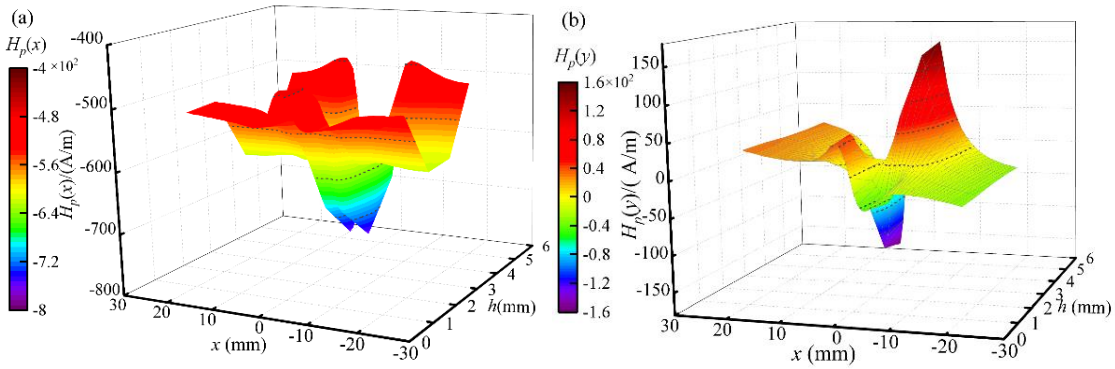

Figure 13. The magnetic field strength of crack defects. (a) Tangential magnetic field strength; (b) normal magnetic field strength.

The gradient of the further extracted magnetic memory signal is shown in Figure 14(a). When the defect depth is 1 mm, the peak value of the normal gradient is small. The gradient value at both ends of the rectangular groove has a small fluctuation when the defect depth is 2 mm. As the defect depth increases to 3 mm, the gradient value at the rectangular groove exhibits an obvious peak. With an increase of the defect depth, the normal magnetic field intensity at both ends of the rectangular groove has an obvious minimum value. A peak value occurs at the center of the geometry at each test. The width of the defect can be roughly estimated by observing the position where the extreme value of the gradient appears, and the variation of the gradient amplitude can be an important reference in the evaluation of the defect depth.

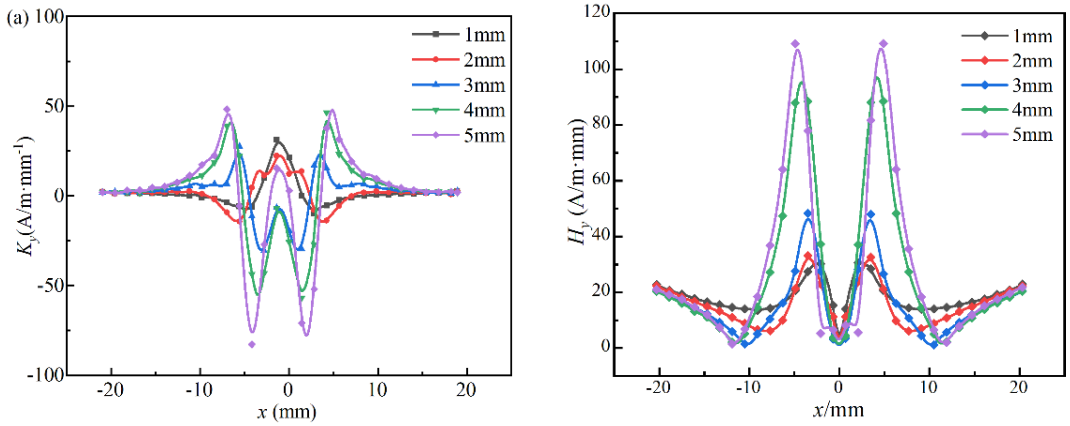

Figure 14. The normal magnetic field characteristic of crack defects. (a) Normal magnetic field gradient; (b) normal magnetic field peak energy.

The magnetic field peak energy of the crack defect is shown in Figure 14(b). It can be seen from the figure that the magnetic field peak energy changes are roughly divided into three stages. In the first stage, when the defect is small, the magnetic field peak energy and the fluctuation range are small. In the second stage, when the defect depth is near 1/2 of the specimen thickness, the magnetic field peak energy amplitude continues to increase. In the third stage, the magnetic field peak energy amplitude continues to increase as the defect depth evolves from 3–4 mm. When the defect is 5 mm, the magnetic field peak energy amplitude is relatively large.

3.3. *Porosity defects*

The stress distribution on the specimen surface is shown in Figure 15, in which the stress is 100 MPa. When the depth of the defect is small, the stress concentration appears on the surface of the specimen, where its shape is a "flake", and the stress value at the porosity is obviously higher than that at other locations. When the depth of the defect increases, the stress in the figure does not significantly change due to the small pore volume. The position of the stress amplitude change coincides with the position of a sudden change of the magnetic memory signal.

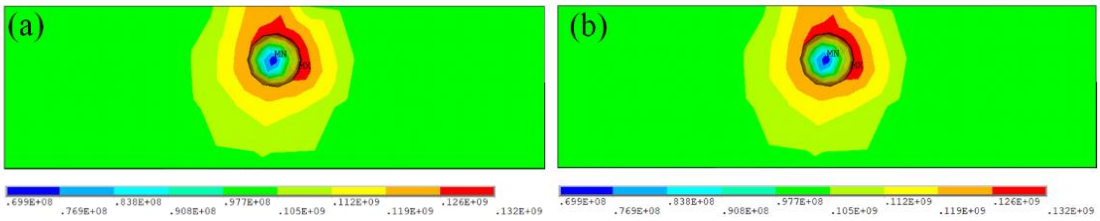

Figure 15. Mises stress distribution. (a) h=1.5mm; (b) h=3mm.

The magnetic memory signals of porosity defects at different depths are shown in Figure 16. The depths are 1.5, 2.5, 3, and 3.5 mm, respectively. Compared with a circular pit and crack defects, the porosity defect size is smaller, so the magnetic memory variation range is correspondingly lower and the wave width is narrower. The magnetic field strength trend along the defect is similar in all different defect depths in both the normal and tangential directions.

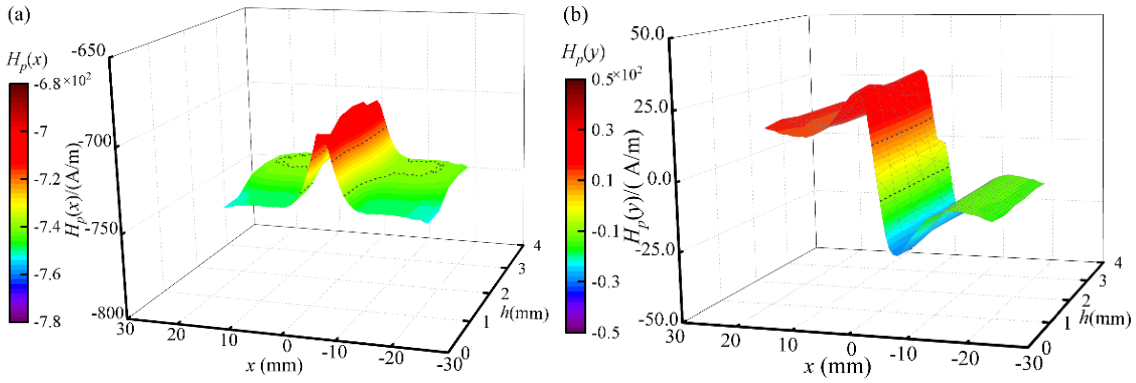

Figure 16. The magnetic field strength of porosity defects. (a) Tangential magnetic field strength; (b) normal magnetic field strength.

The normal magnetic field intensity gradient of porosity defects is shown in Figure 17(a). When the defect is 1.5 mm, the gradient value has a maximum value in the center of the porosity. With an increase of the defect depth, when the depth reaches 2.5 mm, the two endpoints of the porosity fluctuate. When the defect increases to 3 mm, the gradient curve takes the shape of an "M", and two maximum values appear at the two ends of the porosity. When the defect depth is 3.5 mm, the two maximum values increase, and the gradient value at the defect center continues to decrease. When the defect size is constant and the defect depth is less than 1/2 of the plate thickness, the normal magnetic field intensity gradient nominally changes and can only locate the defect range. When the defect reaches 1/2 of the thickness of the plate, it gradually decreases in the center of the defect and gradually increases at both ends of the defect. The location of the defect can be accurately located by analyzing the location of the extreme gradient value.

The porosity normal magnetic field peak energy is shown in Figure 17(b). With an increase of the defect depth, the peak energy gradually decreases. Compared with concave and crack defects, the peak energy variation and amplitude of the porosity defects are smaller. As for the peak energy curves of porosity, there is only a little difference at the defect position, and the curves of the other positions almost coincide. Therefore, by comparing the direction gradient and the magnetic field peak energy of the component association of the magnetic memory signal, we can understand the signal law of different defects, and then complete the classification and identification of the defects.

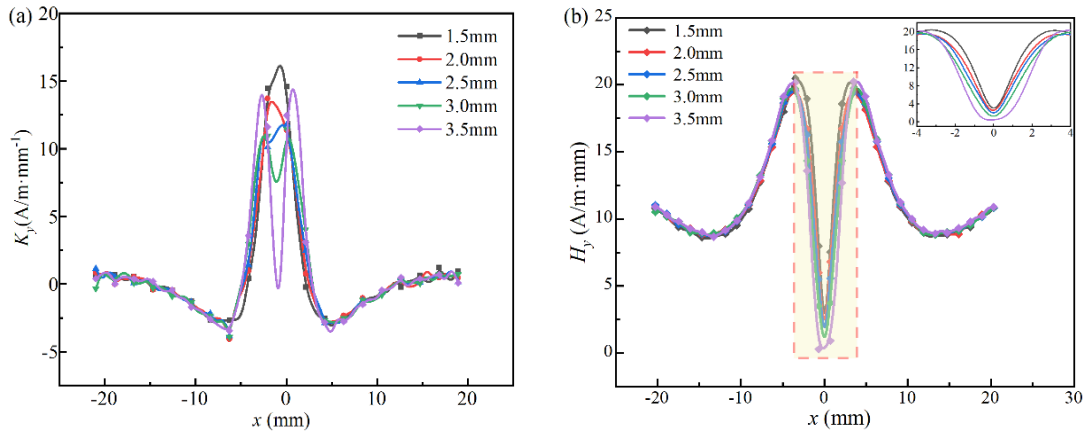

Figure 17. The normal magnetic field characteristic of porosity defects. (a) Normal magnetic field gradient; (b) normal magnetic field peak energy.

3.4. Experiment results

The collected normal signal is processed by wavelet denoising, and the obtained normal magnetic field strength is shown in Figure 18. The experiment data matches well with the tendency of the corresponding numerical data of each defect type, and the peaks and valleys can be obviously seen. The location of the defect can be recognized by the zero-crossing point of the signal. Due to the influence of the factors such as the experimental environment magnetic field and noise signal, the experimental detected signal is larger than the numerical results. The normal magnetic field intensity signal variation range of the pit defects is smaller than that of the crack defects.

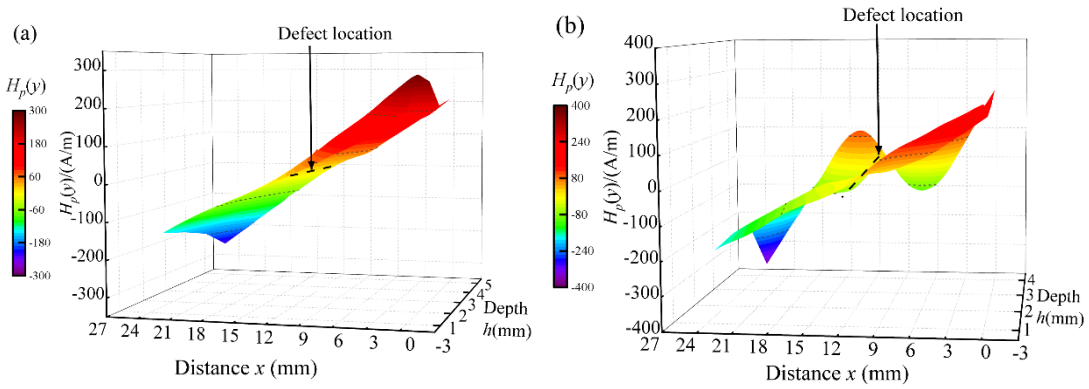

Figure 18. Magnetic memory signal of different defects. (a) Pit normal magnetic field intensity; (b) crack normal magnetic field intensity.

The magnetic field gradient figure is obtained by deriving the signal, as shown in the Figure 19. When the depth of the pit defect is small, the signal fluctuation at the defect is not notable, though the location of the defect can still be found. However, obvious extreme values appear around the defect when the defect depth increases to 4 mm. As to the crack defects shown in Figure 19(b), the gradient signal remains gentle, as the defect depth is below 3 mm. When the defect depth becomes 4 mm, an abrupt increase of the gradient can be observed, and the maximum value appears in the defect center.

In summary, the variation trend and amplitude characteristic of MMM signals show obvious differences among different defect types. Meanwhile, the impact caused by the defect parameters and types are complex, which cannot be decoupled or calculated by a certain formula. If we induced the neutral network, the magnetic field parameters, including $H_{p\text{-}v}$, W, K_y, and H_y, shall be considered in the recognition of defects.

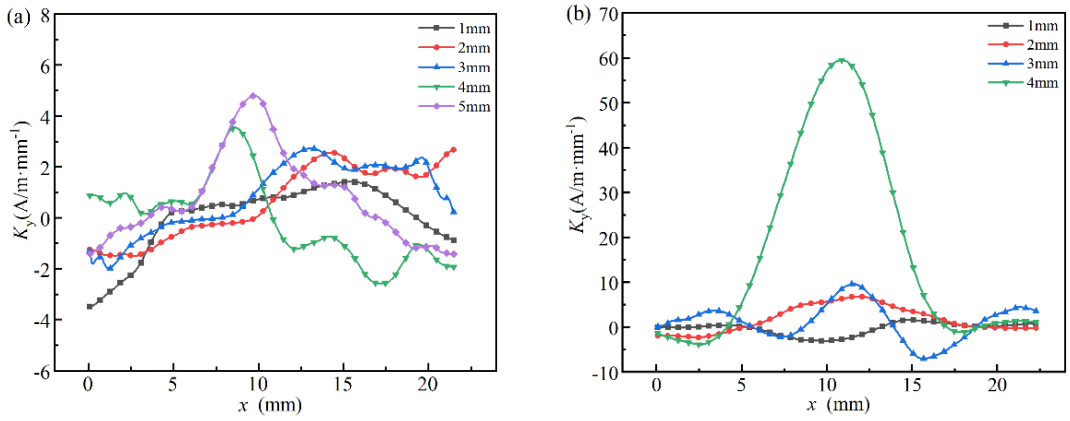

Figure 19. Magnetic field gradient values of different defects. (a) Pits; (b) rectangular defects.

4. Discussion

On the premise of obtaining simulation and experimental data, the characteristic quantities of MMM signals with different defect types have been analyzed in the former section. The four important parameters can be induced into the identification of the defect type, which is the main difficulty in MMM testing. In this section, RBFNN classification and a recognition model with a Gaussian kernel function as the Kohonen function of the model are established to classify and predict three kinds of

defects, such as pits, cracks, and porosity. The average error was used to evaluate the classification and prediction effect of the model. Finally, the confusion matrix data of the training and test sets and the comparison between the predicted and actual values were intuitively displayed by drawing.

The data extracted from the five paths in simulation and experiments is shown in Tables 2–4. The data set consists of 101 groups. Among them, samples 26–29 in Table 2 are experimental data, and the rest are simulation data. For the simulated data set, samples 1–25 were measured at different defect depths, and samples 30–46 were measured at different defect widths. We set 76 groups as the training set and 25 groups as the test set. Because of the complexity and nonlinear characteristics of magnetic memory signals, and according to the change of defect size, the characteristic quantity of the magnetic memory signal will change accordingly. Therefore, according to the waveform variation of the magnetic memory signal, we built a data set around the characteristic quantity.

Table 2. Pit defects sample data.

S_i	$H_{p\text{-}v}$ (A/m) $\times 10^2$	W (m) $\times 10^2$	K_y (A/m• mm^{-1}) $\times 10^2$	H_y (A/m• mm) $\times 10^2$	S_i	$H_{p\text{-}v}$ (A/m) $\times 10^2$	W (m) $\times 10^2$	K_y (A/m• mm^{-1}) $\times 10^2$	H_y (A/m • mm) $\times 10^2$
1	0.571	0.0056	0.168	0. 199	24	0.292	0.006	0.046	0.149
2	0.614	0.0056	0.171	0.209	25	0.627	0.006	0.169	0.210
3	0.598	0.0056	0.178	0.210	26	0.506	0.006	0.130	0.170
4	0.571	0.0056	0.162	0.200	27	0.362	0.006	0.091	0.130
5	0.263	0.0056	0.143	0.185	28	0.118	0.006	–0.017	0.050
6	0.266	0.0056	0.147	0.184	29	-0.332	0.006	–0.121	0.032
7	0.261	0.0056	0.146	0.182	30	-0.725	0.006	–0.229	0.019
8	0.259	0.0056	0.147	0.182	31	0.591	0.006	0.169	0.207
9	0.465	0.0056	0.136	0.161	32	0.325	0.006	0.100	0.184
10	0.412	0.0056	0.101	0.144	33	0.175	0.006	0.052	0.061
11	0.414	0.0056	0.107	0.143	34	0.571	0.006	0.165	0.191
12	0.470	0.0056	0.139	0.163	35	0.558	0.006	0.169	0.200
13	0.378	0.0056	0.110	0.132	36	0.558	0.006	0.150	0.201
14	0.244	0.0056	0.038	0.085	38	0.539	0.006	0.146	0.192
15	0.239	0.0056	0.031	0.084	39	0.216	0.006	0.056	0.076
16	0.385	0.0056	0.104	0.136	40	0.191	0.006	0.045	0.067
17	0.199	0.0056	0.066	0.092	41	0.194	0.006	0.046	0.068
18	–0.118	0.0056	–0.077	0.013	42	0.217	0.006	0.057	0.076
19	–0.077	0.0056	–0.040	0.000	43	0.350	0.006	0.120	0.143
20	0.200	0.0056	0.077	0.090	44	0.328	0.006	0.087	0.125
21	0.305	0.0056	0.040	0.151	45	0.331	0.006	0.086	0.127
22	–0.145	0.0056	0.204	0.054	46	0.351	0.006	0.117	0.144
23	–0.147	0.0056	0.149	0.034					

Table 3. Crack defects sample data.

S_i	$H_{p\text{-}v}$ (A/m) $\times 10^2$	W (m) $\times 10^2$	K_y (A/m• mm^{-1}) $\times 10^2$	H_y (A/m• mm) $\times 10^2$	S_i	$H_{p\text{-}v}$ (A/m) $\times 10^2$	W (m) $\times 10^2$	K_y (A/m• mm^{-1}) $\times 10^2$	H_y (A/m • mm) $\times 10^2$
1	0.811	0.007	0.285	0.282	16	–2.812	0.008	0.447	0.952
2	0.844	0.007	0.308	0.296	17	–3.232	0.009	0.167	1.117
3	0.847	0.007	0.288	0.295	18	–3.116	0.009	0.166	1.081
4	0.807	0.007	0.269	0.283	19	–3.069	0.009	0.166	1.079
5	0.891	0.007	0.205	0.315	20	–3.139	0.009	0.143	1.106
6	0.943	0.007	0.240	0.329	21	0.405	0.007	0.041	0.781
7	0.952	0.007	0.239	0.331	22	0.844	0.007	0.086	0.906
8	0.934	0.007	0.194	0.319	23	1.286	0.007	0.097	1.161
9	–1.445	0.007	0.246	0.514	24	1.471	0.008	0.151	1.298
10	–1.392	0.007	0.274	0.494	25	2.023	0.008	0.159	1.456
11	–1.420	0.007	0.249	0.499	26	1.030	0.007	–0.031	0.034
12	–1.420	0.007	0.279	0.497	27	0.360	0.007	0.063	0.016
13	–2.808	0.008	0.463	0.975	28	1.255	0.007	0.096	0.046
14	–2.806	0.008	0.423	0.975	29	-1.976	0.007	0.595	0.081
15	–2.861	0.008	0.508	0.986					

Table 4. Porosity defects sample data.

S_i	$H_{p\text{-}v}$ (A/m) $\times 10^2$	W (m) $\times 10^2$	K_y (A/m•m m^{-1}) $\times 10^2$	H_y (A• m^{-1}• mm) $\times 10^2$	S_i	$H_{p\text{-}v}$ (A/m) $\times 10^2$	W (m) $\times 10^2$	K_y (A/m•m m^{-1}) $\times 10^2$	H_y (A• m^{-1}• mm) $\times 10^2$
1	0.547	0.004	0.155	0.190	14	0.534	0.004	0.127	0.186
2	0.577	0.004	0.185	0.202	15	0.533	0.004	0.128	0.186
3	0.573	0.004	0.168	0.201	16	0.539	0.004	0.166	0.187
4	0.548	0.004	0.156	0.193	17	0.532	0.004	0.156	0.185
5	0.538	0.004	0.156	0.187	18	0.530	0.004	0.114	0.186
6	0.552	0.004	0.149	0.194	19	0.528	0.004	0.124	0.185
7	0.552	0.004	0.150	0.192	20	0.526	0.004	0.160	0.182
8	0.537	0.004	0.151	0.187	21	0.581	0.004	0.150	0.205
9	0.536	0.004	0.153	0.186	22	0.558	0.004	0.134	0.196
10	0.544	0.004	0.138	0.191	23	0.556	0.004	0.109	0.196
11	0.544	0.004	0.136	0.190	24	0.564	0.004	0.071	0.197
12	0.534	0.004	0.167	0.187	25	0.578	0.004	0.013	0.202
13	0.533	0.004	0.158	0.187					

The input vector is composed of different eigenvalues, including the peak and trough values of the normal magnetic field intensity, the wave width, the normal magnetic field gradient, and the normal magnetic field peak energy $\{H_{p\text{-}v}; W; K_y; H_y\}$. The output vector consists of three defect types: pit, crack, and porosity, among which the pit defect is class 1, the crack defect is class 2, and the porosity

defect is class 3. The data set is imported into the Matlab editor, the data set is scrambled and divided into the training and test sets, and then the data is normalized to reduce the error. The RBFNN system is set up, the network is tested, and then the simulation test is carried out. The data is reverse-normalized. Finally, the average error is used to evaluate the network performance. The confusion matrix data is obtained, as shown in Figure 20, and the comparison between the predicted value and the actual value is shown in Figure 21.

The confusion matrix of the RBFNN is shown in Figure 20. Each column in the confusion matrix represents the prediction category, the total number of each column represents the number of data predicted for that category, and each row represents the true belonging category of the data. As can be seen from the confusion matrix of the training set in Figure 20(a), the first line indicates that the classification of the 36 samples of class 1 pit defects is correct. Among the 22 samples of class 2, 21 samples were correctly classified and 1 sample was classified incorrectly. The network classified the crack defect errors into the pit defect. The third line indicates that 18 samples of the class 3 porosity defects are correctly classified. Similarly, it can be seen from the confusion matrix of the test set in Figure 20(b) that the classification of the 9 samples of class 1 is correct. The 7 categories of class 2 are correct. The 7 samples of class 3 are correctly classified.

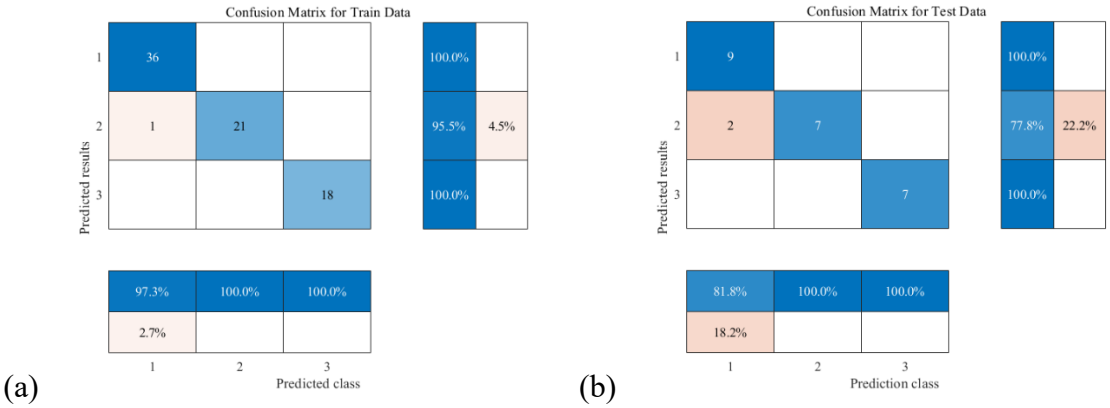

(a) (b)

Figure 20. Confusion matrix. (a) Training set confusion matrix; (b) test set confusion matrix.

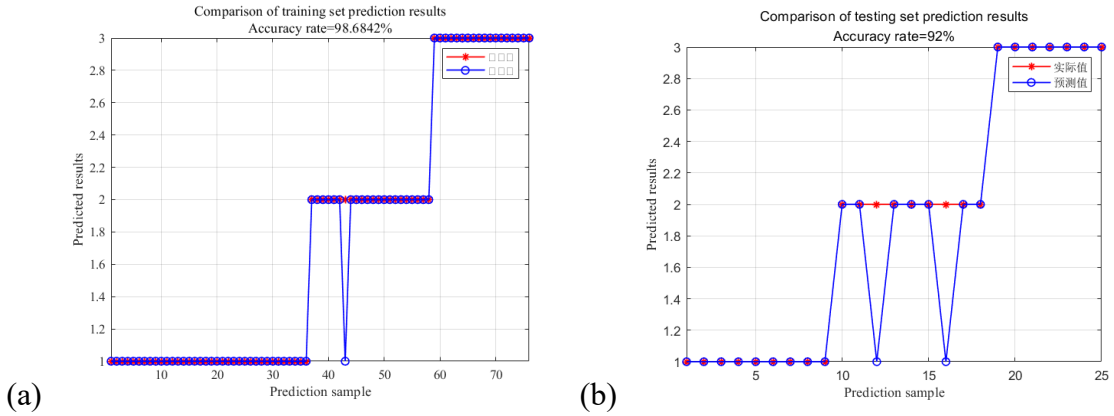

(a) (b)

Figure 21. Comparison result of actual value and predicted value: (a) Comparison result graph of training set; (b) comparison result graph of test sets.

The comparison between the actual value and the predicted value is shown in Figure 21. It can be

seen in Figure 21(a) that the accuracy of the prediction results of the training set is 98.68%, and the prediction of the network pits, cracks, and porosity defects is correct. As can be seen from Figure 21(b), the accuracy of the prediction results of the test set is 92%, and the prediction of the three defects is correct. In general, the established RBFNN can basically predict the type of defects; however, in practical applications, this model will be limited by the sample data, and more data needs to be accumulated to further extract multiple feature quantities and analyze its feature law, so as to accurately predict defects and improve the prediction effect of the model.

5. Conclusions

According to the theory of energy conservation and electromagnetic fields, a metal magnetic memory detection model based on three-dimensional force-magnetic coupling analysis was established, and the characteristic quantity changes of different defect types and depths were compared and analyzed. Finally, an RBFNN network is established to realize the classification prediction. The main conclusions are as follows:

(1) The numerical calculation results show that for the three types of defects, when the defect depth was less than 50% of the specimen thickness, the signal gradient and peak energy changes were small. The defect depth was greater than or equal to 50% of the specimen thickness, and the two characteristic curves of the gradient and energy could reflect the defect location and width.

(2) The experimental results showed that the magnetic field strength of the crack defects varies greatly varied compared with the pit, and the gradient value had a maximum value at the defect. The correctness of the simulation was verified by the experiment, and the data were accumulated for the subsequent pattern recognition.

(3) To solve the problem that pattern recognition and defect classification could not be realized in MMM detection, four characteristic quantities were selected: Signal peak and valley $H_{p\text{-}v}$, signal width W, gradient K_y, and peak energy H_y. An RBFNN was established to realize an intelligent defect classification. It proved that the accuracy of both the training and test sets were 100%. The results showed that the selected feature quantity was effective and the network could complete the defect prediction.

The intelligent recognition method of MMM testing can be used in the quick detection of pressure vessels and pipes, which can reduce the cost of the detection. Although lots of test data were included in this study to build the data set, there are still many factors that should be considered in the practical tests. The problem will be solved as the online detection data are induced to train the network.

Use of AI tools declaration

The authors declare they have not used Artificial Intelligence (AI) tools in the creation of this article.

Acknowledgments

The work was supported by Science and Technology Innovation Projects of Zhejiang Academy of Special Equipment Science (ZTJ-201301012).

Conflict of interest

The authors declare that they have no known competing interests.

References

1. Z. Xiao, C. Zhang, P. Li, Engineering oxygen vacancies on Tb-doped ceria supported Pt catalyst for hydrogen production through steam reforming of long-chain hydrocarbon fuels, *Chinese J. Chem. Eng.*, 68 (2024). https://doi.org/10.1016/j.cjche.2023.12.008
2. Q. Ma, G. Tian, Y. Zeng, R. Li, H. Song, Z. Wang, et al., Pipeline in-line inspection method, instrumentation and data management, *Sensors*, **21** (2021), 3862. https://doi.org/10.3390/s21113862
3. K. Xu, X. Qiu, X. Tian, Theoretical investigation of metal magnetic memory testing technique for detection of magnetic flux leakage signals from buried defect, *Nondestruct. Test. Eva.*, **33** (2018), 45–55. https://doi.org/10.1080/10589759.2017.1293050
4. S. K. A. D. Steklov, Assessment of welded joints stress-strain state inhomogeneity before and after post weld heat treatment based on the metal magnetic memory method, *Weld. World*, **60** (2016), 665–672. https://doi.org/10.1007/s40194-016-0335-7
5. Y. Yang, X. Ma, S. Su, W. Wang, Study on corrosion damage characterization and tensile strength evaluation for locally corroded bridge steel via metal magnetic memory method, *Measurement*, **207** (2023), 112406. https://doi.org/10.1016/j.measurement.2022.112406
6. B. Liu, J. Sun, L. He, H. Geng, L. Yang, Quantitative study on internal detection signal of weak magnetic stress in oil and gas pipelines based on force-magnetic Noncoaxial effect, *Measurement*, **215** (2023), 112870. https://doi.org/10.1016/j.measurement.2023.112870
7. F. Gao, J. Fan, L. Zhang, Magnetic crawler climbing detection robot basing on metal magnetic memory testing technology, *Robot. Auton. Syst.*, **125** (2020), 103439. https://doi.org/10.1016/j.robot.2020.103439
8. S. Kolokolnikov, A. Dubov, A. Medvedev, D. Boriskin, Comprehensive inspection of refrigerated ammonia storage tank welded joints by the metal magnetic memory technique and conventional NDT methods, *Weld. world*, **64** (2020), 1659–1670. https://doi.org/10.1007/s40194-020-00938-8
9. X. Di, W. Li, S. Bai, Metal magnetic memory signal by neural network for welding cracks, *T. China Weld. Inst.*, **3** (2008), 13–16. https://doi.org/10.1109/IEMBS.1993.978529
10. H. Chen, C. Wang, H. Zhu, Metal magnetic memory test method based on magnetic gradient tensor, *Chinese J. Sci. Instrum.*, **37** (2016), 602–609. https://doi.org/10.3969/j.issn.0254-3087.2016.03.017
11. X. D. Shi, J. C. Fan, W. Zhou, Pattern recognition of pipeline magnetic memory inspection based on BP neural network, *China Petrol. Mach.*, **48** (2020), 111–117. https://doi.org/10.16082/j.cnki.issn.1001-4578.2020.06.017
12. P. Ramuhalli, L. Udpa, S. S. Udpa, Electromagnetic NDE signal inversion by function-approximation neural networks, *IEEE T. Magn.*, **38** (2002), 3633–3642. https://doi.org/10.1109/TMAG.2002.804817
13. A. F. Joshi, L. Udpa, S. Udpa, Adaptive wavelets for characterizing magnetic flux leakage signals from pipeline inspection, *IEEE T. Magn.*, **42** (2006), 3168–3170. https://doi.org/10.1109/INTMAG.2006.376376
14. H. Zhang, X. Yu, Research on oil and gas pipeline defect recognition based on IPSO for RBF neural network, *Sustain. Comput.-Infor.*, **20** (2018), 203–209. https://doi.org/10.1016/j.suscom.2017.08.002
15. S. Wang, H. L. Huang, G. Han, Quantitative evaluation of magnetic memory signal based on PCA & GA-BP neural network, *J. Electronic Meas. Instrum.*, **32** (2018), 190–196. https://doi.org/10.13382/j.jemi.2018.10.026
16. H. Y. Xing, Y. H. Chen, X. F. Li, Magnetic memory identification model of mental weld defect levels based on dynamic immune fuzzy clustering, *Chinese J. Sci. Instrum.*, **40** (2019), 225–232. https://doi.org/10.19650/j.cnki.cjsi.J1905312

17. P. Shi, K. Jin, P. Zhang, S. Xie; Z. Chen; X. Zheng, Quantitative inversion of stress and crack in ferromagnetic materials based on metal magnetic memory method, *IEEE T. Magn.*, **54** (2018), 1–11. https://doi.org/10.1109/TMAG.2018.2856894
18. K. Yao, B. Deng, Z. D. Wang, Numerical studies to signal characteristics with the metal magnetic memory-effect in plastically deformed samples, *NDT & E Int.*, **47** (2012), 7–17. https://doi.org/10.1016/j.ndteint.2011.12.004
19. P. P. S, X. J. Z. Magnetic charge model for 3D MMM signals, *Nondestruct. Test. Eva.*, **31** (2016), 45–60. https://doi.org/10.1080/10589759.2015.1064121
20. B. Liu, Y. Fu, B. Xu, Study on metal magnetic memory testing mechanism, *Res. Nondestruct. Eva.*, **26** (2015), 1–12. https://doi.org/10.1080/09349847.2014.896965
21. A. Wenger, E. Török, Theory of the Magnetomechanical pole effect, *J. Magn. Magn. Mater.*, **13** (1979), 283–288. https://doi.org/10.1016/0304-8853(79)90210-5
22. M. Shi, Y. Liang, M. Zhang, Z. Huang, L. Feng, Z. Zhou, Pipeline damage detection based on metal magnetic memory, *IEEE T. Magn.*, **57** (2021), 1–15. https://doi.org/10.1109/TMAG.2021.3084808
23. Y. En, L. Luming, C. Xing, Magnetic field aberration induced by cycle stress, *J. Magn. Magn. Mater.*, **312** (2007), 72–77. https://doi.org/10.1016/j.jmmm.2006.09.019
24. A. Dubov, S. Kolokolnikov, Detection of cracks in 25Cr35NiNb ethylene pyrolysis furnace tubes by metal magnetic memory technique, *Weld. World*, **58** (2014), 225–236. https://doi.org/10.1007/s40194-013-0102-y
25. L. Wu, K. Yao, P. Shi, B. Zhao, Y. S. Wang, Influence of inhomogeneous stress on biaxial 3D magnetic flux leakage signals, *NDT & E Int.*, **109** (2020), 102178. https://doi.org/10.1016/j.ndteint.2019.102178
26. G. Han, H. Huang, A dual-dipole model for stress concentration evaluation based on magnetic scalar potential analysis, *NDT & E Int.*, **118** (2021), 102394. https://doi.org/10.1016/j.ndteint.2020.102394
27. X. Jian, X. Jian, G. Deng, Experiment on relationship between the magnetic gradient of low-carbon steel and its stress, *J. Magn. Magn. Mater.*, **321** (2009), 3600–3606. https://doi.org/10.1016/j.jmmm.2009.06.077
28. K. Xu, K. Yang, J. Liu, Y. Wang, Study on metal magnetic memory signal of buried defect in fracture process, *J. Magn. Magn. Mater.*, **498** (2020), 166139. https://doi.org/10.1016/j.jmmm.2019.166139
29. S. Bao, P. Jin, Z. Zhao, M. Fu, A review of the metal magnetic memory method, *J. Nondestruct. Eva.*, **39** (2020), 11. https://doi.org 10.1007/s10921-020-0652-z
30. K. Xu, J. Liu, K. Yang, J. Liu, Effect of applied load and thermal treatment on the magnetic memory signal of defect-bearing Q345R steel samples, *J. Magn. Magn. Mater.*, **539** (2021), 168366. https://doi.org/10.1016/j.jmmm.2021.168366
31. C. Pang, J. Zhou, R. Zhao, H. Ma, Y. Zhou, Research on internal force detection method of steel bar in elastic and yielding stage based on metal magnetic memory, *Materials*, **12** (2019), 1167. https://doi.org/10.3390/ma12071167
32. M. Moonesan, M. Kashefi, Effect of sample initial magnetic field on the metal magnetic memory NDT result, *J. Magn. Magn. Mater.*, **460** (2018), 285–291. https://doi.org/10.1016/j.jmmm.2018.04.006